PAPER

High-energy ion (He^{+}, Si^{++}, Ga^{+}, Au^{++}) interactions with PMMA in ion beam lithography

IOP Publishing Nanotechnology

Nanotechnology **31** (2020) 325301 (8pp) https://doi.org/10.1088/1361-6528/ab8d69

High-energy ion (He^+, Si^{++}, Ga^+, Au^{++}) interactions with PMMA in ion beam lithography

Lei Zhang, Joseph P Thomas, Xiaoyi Guan, Nina F Heinig and Kam Tong Leung

WATLab, and Department of Chemistry, University of Waterloo, Waterloo, Ontario N2L 3G1, Canada

E-mail: tong@uwaterloo.ca

Received 7 February 2020, revised 25 March 2020
Accepted for publication 27 April 2020
Published 28 May 2020

Abstract

Resist-based ion beam lithography has been studied by exposing different species of ions (He^+, Si^{++}, Ga^+ and Au^{++}) on 700 and 2000 Å thick poly(methyl methacrylate) (or PMMA) films supported on Si substrates. By comparing the resist sensitivities to different ions and the cross-sectional shapes of the developed features with the simulation outputs from the TRIM (TRansport of Ions in Matter) software, long-chain scissoring in PMMA can be largely attributed to ion-initiated electron cascades (as evaluated by ion energy loss to the electrons) and recoil atom cascades (as evaluated by vacancy distribution in TRIM). The ion-initiated electron cascades contribute more to the resist sensitivity for the lighter ions, while the recoil atom cascades are more important for the heavier ions. A proportional relation between the resist sensitivity and the product of the ion energy loss to electrons and vacancy number is obtained semi-empirically for heavy ions. The He^+ ion is the only ion species that can travel through and therefore expose the entire 2000-Å thick PMMA resist film, while the heaviest ion, Au^{++}, provides the highest resist sensitivity. The effective energy and momentum impartment to the resist by the ion, as revealed by recoil atom cascades and vacancy formation, is important to significantly expanding the material types suitable for ion beam lithography.

Supplementary material for this article is available online

Keywords: focused ion beam, ion beam lithography, PMMA, transport of ions in matter simulation

Some figures may appear in colour only in the online journal

1. Introduction

With the continuing development of focused ion beam (FIB) microscopy particularly in imaging and patterning resolutions, expansion of the types of ion sources and ion species, and combination with other techniques, FIB microscopy has now been extensively employed in various analytical and manufacturing fields, including nano-device prototyping, circuit editing and reverse engineering [1–7]. For a high-resolution scanning FIB microscope, two types of ion sources are commonly used: gas field ion source (GFIS) and liquid metal ion source (LMIS). In a GFIS, ions are generated by field-ionizing incoming gaseous atoms (He, Ne) in a high electrical field in the vicinity of a tungsten tip so sharp that only three atoms (a trimer) are present at the tip apex [8, 9]. In a LMIS, ions are emitted from the Taylor cone of the liquid metal, which is formed when a high voltage (~10 kV) is applied between an extractor and the liquid metal wetted tip [10–13]. The working principles of these ion sources, together with some of their characteristics, are shown schematically in figure 1. The He^+ ion beam generated from a GFIS has three orders of magnitude higher brilliance (in A $cm^{-2}sr$) than the Ga^+ LMIS [8]. However, there are two disadvantages that limit its widespread usage: (1) to date the only available ion species in a commercial FIB

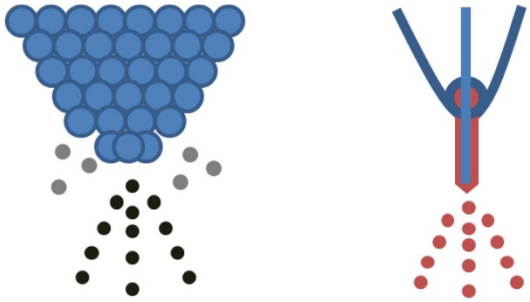

	Helium GFIS	Gallium LMIS	AuSi LMAIS
Maximum beam energy:	50 keV	30 keV	80 keV
Maximum beam current:	150 pA	20000 pA	500 pA (Si^{++}); 2500 pA (Au^{++})
Minimum beam spot size:	3.5 Å	25 Å	80 Å (Si^{++}); 120 Å (Au^{++})

Figure 1. Schematic diagrams of Helium gas field ion source (GFIS), and of Gallium liquid metal ion source (LMIS) and AuSi liquid metallic alloy ion source (LMAIS), and their typical operating characteristics.

microscope are based on He^+ and Ne^+; and (2) the trimer at the tip only lasts a couple of weeks at most and needs to regenerate, and there is a continued degradation of the beam current often rapidly in the short period after the trimer is formed. This latter aspect limits the time frame of any experiment that requires beam stability over an extended period of time. Understandably, the LMIS is considerably more popular in FIB because the LMIS could easily overcome these limitations of the GFIS. For a LMIS, there is a broad range of ion species (nearly half of the elements in the periodic table) from light ion such as Be^+ to heavy ion such as Bi^+. Furthermore, the metallic ion species can come from not just elemental metals but indeed metal alloys (binary or ternary alloys at appropriate eutectic concentrations) [1, 13]. A LMIS can also last as long as there is metal in the reservoir (before it needs to be re-filled), which is significantly longer than the 40 weeks afforded by 20 newly generated trimers, each with a 2 week lifetime, typically obtainable from a GFIS. More importantly, the ion beam so generated is stable over a significantly longer contiguous period of time than a trimer from a GFIS, making the LMIS much more viable for large-area or extended lithography application.

Resist-based ion beam lithography (IBL), although not as popular and well-developed as optical lithography and electron beam lithography (EBL), has attracted much recent attention because of its high resolution, high resist sensitivity and negligible proximity effects [14–17]. In comparison with electron beams, ion beams also have additional unique capabilities such as milling and doping, which makes a FIB microscope more versatile in a manufacturing process than an electron microscope. Poly(methyl methacrylate) (or PMMA) is one of the most frequently used resists in EBL. The electron-PMMA interaction process is well known: the long chain in PMMA is scissored into developer-soluble smaller chains by high-energy electrons, which include the primary electrons emitted from the electron source and focused by the lenses, the secondary electrons generated inside the PMMA polymer as the primary electrons forwardly scatter inside the film and ionize the polymer, and the backscattered electrons when the primary electrons are backscattered by atomic nuclei in the substrate [18]. When a primary electron collides with a target, any secondary electron(s) ejected from the target could further collide with and knock out electrons from nearby targets. In this way, the primary electron initiates an electron cascade. The spatial range and geometrical profile of the electron cascade determine the depth and lateral dimension of the electron exposure (which is sometimes called the probe volume). Evidently, the PMMA-based IBL is more complicated than EBL, because ions can activate not only the electron cascade, just as the primary electrons in EBL, but also the recoil atom cascade. The latter is the result of displacement of atoms (H, C, O) in PMMA caused by high-energy ion collisions and momentum impartment. If electron removal can cause long-chain scissoring, atom removal (i.e. generation of vacancies in the material lattice) can obviously make long-chain scissoring not just viable but indeed more efficient. This enhanced efficiency has enabled orders of magnitude lower dose needed in IBL than EBL to expose the same resist [14, 17].

The high-energy ion-matter interaction process can be studied by using the TRIM (TRansport of Ions in Matter) program, which uses the Monte Carlo method to simulate the ion-atom collisions to generate the recoil atom cascade [19]. In addition to furnishing a direct view of the trajectories of the incident ion and recoil atoms and of their stopping sites in a selected material, TRIM also provides useful calculated parameters such as ion ranges, ion energy losses to phonons, electrons and recoil atoms, and vacancy numbers. Here, we expose high-energy He^+, Si^{++}, Ga^+ and Au^{++} ion beams to write a test pattern consisting of a series of straight lines on a 700-Å and a 2000-Å thick PMMA layers deposited on Si substrates. In each case of the ion beams, we then examine the cross sections of the developed lines with scanning electron microscopy (SEM) to evaluate the resist sensitivity, i.e. the dissolved volume caused by an ion ($Å^3$/ion). (Although Si^+ and Au^+ ion beams are also available, they generally exhibit larger beam spots than their respective doubly charged ions, therefore making them less desirable for lithography application.) We further compare our experimental results with the TRIM simulations for exposures

of these different ions. To account for the long-chain scissoring by ion-induced and recoil atom-induced electrons (similar to secondary electrons in EBL), we obtain the 'ionization' data in TRIM, i.e. energy losses to electrons by incident ion and by recoil atoms. To account for the long-chain scissoring by H, C and O atom displacement, we also determine the number of vacancies (or vacancy number) as a function of depth. From the Ga^+ and Au^{++} exposure study, the resist sensitivity is found to be proportional to the product of the ion energy loss to electrons and vacancy number. Furthermore, the cross-sectional shapes of the developed lines in the 2000-Å thick PMMA are discernibly different for different incident ions: pear shape for He^+, Florence flask shape for Si^{++} and trench shape for Ga^+ and Au^{++}. This indicates that long-chain scissoring is mainly driven by ion-initiated electron cascade for He^+, with increasing contribution from the recoil atom cascade for the heavier incident ions.

2. Experimental and simulation details

Si(100) chips (5 mm × 10 mm in size, 0.5 mm thick, p-type) with native oxide were degreased and sequentially cleaned by sonication in acetone, isopropyl alcohol (IPA) and deionized water, each for 10 min, and dried by nitrogen gas. PMMA A2 and A4 with a molecular weight of 950 kDa (MicroChem Corp.) were then spin-coated at 4000 rpm onto the Si substrates to give a 700-Å and a 2000-Å thick films, respectively. The film thicknesses measured by atomic force microscopy (AFM) are 70 ± 5 and 200 ± 10 nm, respectively. It should be noted that we use the unit of Å instead of nm here, because it is more consistent with the TRIM program, which does not provide the nm unit. After spin-coating, the Si chips were baked at 180 °C on a hot plate for 90 s. The ion beam exposures were performed in three separate instruments in our laboratory: a Zeiss Orion Plus helium ion microscope equipped with a pattern generator developed by Fibics Inc. for He^+ [20]; a Zeiss Auriga dual-beam FIB-SEM workstation also equipped with the Fibics pattern generator for Ga^+; and a Raith ionLine ion beam lithography system for Si^{++} and Au^{++} [21]. Sets of parallel lines (500 μm long for He^+ and Ga^+, 1 mm long for Si^{++} and Au^{++}) were patterned onto the PMMA films with a series of doses. The beam (or probe) currents delivered to the sample were 0.9, 2.1, 2.1 and 3.2 pA (measured by a Faraday cup, all using a 10 μm diameter objective lens or mass selecting aperture) for He^+, Si^{++}, Ga^+ and Au^{++}, respectively, and the corresponding beam energies were 43, 70, 30 and 70 keV for He^+, Si^{++}, Ga^+ and Au^{++}, respectively. As we intend to obtain the highest lithography resolution, the choice of these energies for the ions is based on the highest imaging and milling resolutions obtainable in their respective instruments. It should be noted that as the voltage applied on the liquid metal alloy ion source to generate Si^{++} and Au^{++} was 35 kV, the effective beam energy for the doubly charged ions was therefore doubled. Furthermore, when converting the dose unit from pA cm^{-1} to ions/cm, a coefficient of 0.5 should be applied to the doubly charged ions. A short line was cut on the Si surface before PMMA spin coating. After the focus of the ion beam was optimized at the end of the pre-cut line, we performed the exposure 100 μm away. Typically, the ion exposure time for a 500 μm line was less than 1 s, while the write time that also included the pattern generator calculation time and stage movement time (in the Raith ionLine system) was a few seconds. After exposure, the samples were developed in a MIBK:IPA (1:3) solution (MicroChem Corp.) at room temperature for 30 s, and then rinsed in IPA for 30 s. A 60-Å thick Au/Pd thin film was sputter-coated on the sample surface to enhance its electrical conductivity for SEM measurement. After immersing in liquid N_2 for 60 s, the Si chip was cleaved along the pre-cut short line, which was used as a reference mark in the line patterning process to ensure that the Si was cleaved across the patterned lines. The cross section of the developed lines was examined in a Zeiss Merlin SEM with a 10 keV beam energy.

The simulation was performed by using the TRIM program in the SRIM (Stopping and Range of Ions in Matter) software package (version 2013) [19]. The ion data input included ion species and its energy, while the target system inputs corresponding to the two experimental samples were 700-Å PMMA on 2000-Å Si, and 2000-Å PMMA on 2000-Å Si. The simulation was carried out using detailed calculation in full damage cascades mode. A total number of 2000 ions were used for the calculation in order to obtain good statistics. The trajectory of each ion in the target was followed and examined. A high-energy incident ion could eject electrons and recoil atoms, with the former quantified as 'ionization-energy loss to electrons by ions' and the latter as 'energy loss to recoils' and 'knock-on vacancies' in TRIM. Subsequently, the emitted electrons, if given sufficiently high energy, could undergo further transport inside the film and eject other electrons, causing an electron cascade similar to that occurs in EBL. Unfortunately, this process was not tracked by TRIM. On the other hand, the emitted recoil atom, if given sufficiently high energy, could also transport inside the film and could knock out not just recoil atoms but also electrons, causing both recoil cascade and electron cascade (the latter of which is considered second order when compared with the ion-initiated electron cascade in terms of sequence and energy). The trajectories of the emitted atoms (H, C, O and Si) and their vacancy numbers were recorded. The energy loss to electrons by recoils was quantified as 'ionization-energy loss to electrons by recoils' in TRIM. It is worth noting that if the ion or a recoil atom collide with an atom but does not have sufficient energy to displace it, the energy imparted to the atom would be represented by 'energy loss to phonons', which could amount to 50% of the initial ion energy for heavy ions. We compare these simulation data with the experimental results (on the resist sensitivity and cross-sectional shape of the developed line) to gain insight into the ion-PMMA interaction process that governs the final lithography results.

3. Results and discussion

Figure 2 compares the experimental and simulation results for He^+, Si^{++}, Ga^+ and Au^{++} ion exposures on the supported 700-Å thick PMMA film. The top panels show the SEM

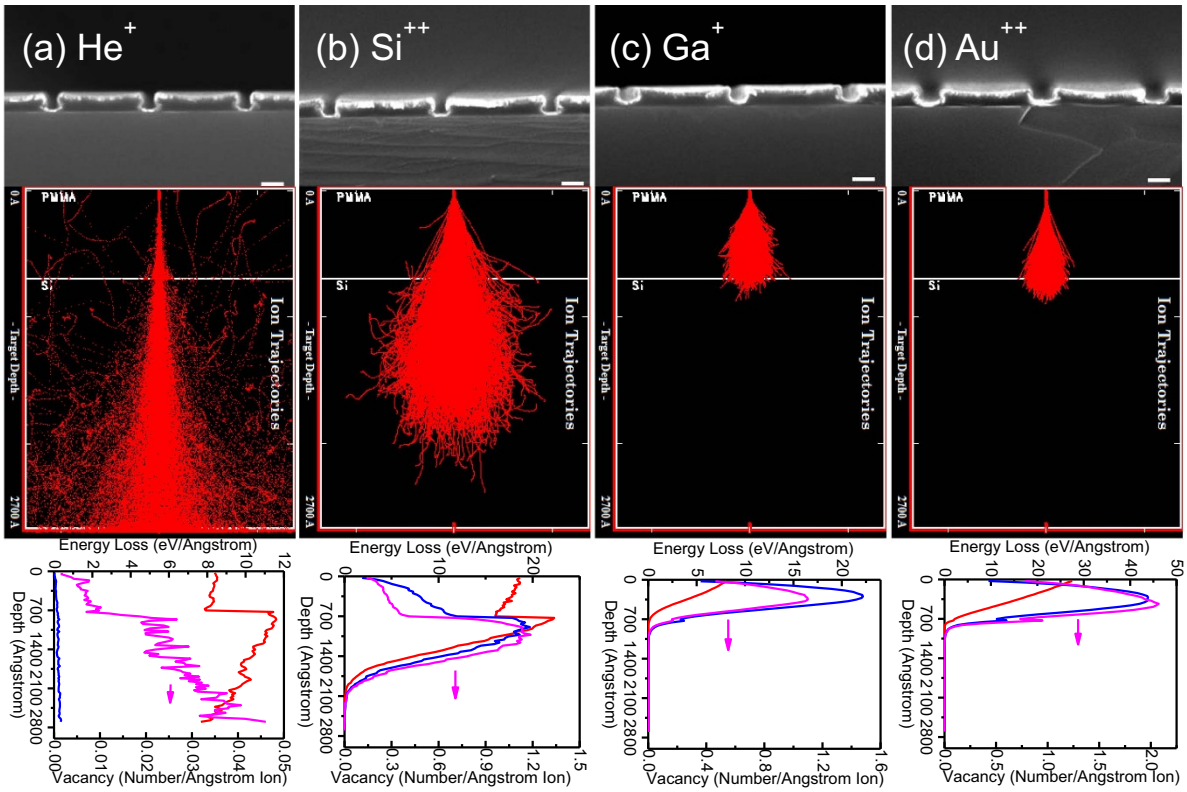

Figure 2. Top: SEM images of cross sections of developed lines on a 700-Å thick PMMA film patterned by (a) He^{+} at 43 keV, dose: 9.0×10^{7} ions cm^{-1}; (b) Si^{++} at 70 keV, dose: 3.1×10^{7} ions cm^{-1}; (c) Ga^{+} at 30 keV, dose: 2.6×10^{8} ions cm^{-1}, and (d) Au^{++} at 70 keV, dose: 2.8×10^{7} ions cm^{-1}. The scale bar represents 100 nm. Middle: Simulated ion trajectories provided by TRIM. Bottom: Depth profiles of energy loss to electrons by ion (red), energy loss to electrons by recoil atoms (blue), and vacancy number (magenta).

images of cross sections of the developed lines; the center panels show the ion trajectories in the sample; and the bottom panels show the depth profiles of ionization energy loss and vacancy data. The depth profiles of ionization energy loss correspond to the amounts of energy loss to electrons by an incident ion (in red colour) or recoil atoms (in blue) when the respective ion or recoil atoms travel one Angstrom distance at different depth. The vacancy depth profiles correspond to the sum of H, C and O vacancies caused by both the incident ion (knock-on) and recoils when they transport one Angstrom distance at different depth (in magenta colour). For each ion species, we have patterned the lines with a series of doses and obtained the cross-sectional SEM images of the developed lines. With increasing doses, the depths of the developed lines appear to increase correspondingly until the entire film is exposed for the light ions or until an apparent depth limit is reached in the film for the heavy ions. Further increasing the dose enlarges the line width, and even leads to overdosed un-dissolved parts in the cross section of the developed lines. We have chosen to display in figure 2 (top panels) the patterns with the appropriate minimal dose for which the developed line has just been completely through the PMMA film for He^{+} and Si^{++} or has just reached its depth limit for Ga^{+} and Au^{++}. He^{+} and Si^{++} ions are capable of exposing completely through the entire 700-Å thick PMMA film with 9.0×10^{7} and 3.1×10^{7} ions cm^{-1}, respectively, apparently due to their small atomic masses and therefore long travel distances as revealed in the ion trajectory simulation (> 2700 Å for He^{+}, ~2000 Å for Si^{++}). In contrast, the PMMA film is not thoroughly exposed by the heavier ions of Ga^{+} and Au^{++}, with their depth limits reached with respective doses of 2.6×10^{8} and 2.8×10^{7} ions cm^{-1}. In their respective SEM images, about 100 and 50 Å thick layers of the respective PMMA films under the lines are not dissolved, which cause the entire metallised patterned layers to be removed after lift-off in acetone. In the corresponding ion trajectory simulation results (figures 2(c) and (d), middle panels), there are indeed considerably less ions reaching the bottom of the PMMA film.

The corresponding line widths of the developed lines are measured to be 600, 600, 1000, 1100 Å for He^{+}, Si^{++}, Ga^{+} and Au^{++} ions, respectively. It should be noted that the respective sizes of the beam spots for optimal beam conditions as commissioned by the manufacturers are 3.5, 80, 25 and 120 Å, and the developed lines are therefore considerably wider than the ion beam spots. The line width (and correspondingly the probe volume in three dimensions) is caused by the ion-PMMA interaction process, which depends on other factors such as the ion trajectory, ion-induced electron and recoil cascades in addition to the beam-spot size. In spite of the difficulty to quantify the contributions of individual factors to the line width, because of the lack of beam spot measurement and of the inaccessible electron cascade information in TRIM, we can draw some general conclusions from the

Table 1. Experimental and simulated results of ion exposures on 700-Å and 2000-Å thick PMMA films. All simulated results (energy loss to electrons by ion, energy loss to electrons by recoils, energy loss to recoils by ion, and vacancy number per ion) are obtained by integrating their corresponding depth profiles over the entire thickness of the PMMA film.

Ion Species	Energy (keV)	Momentum (Kg · m s^{-1})	Energy loss to electrons per ion (eV)	Energy loss to electrons by recoils (eV)	Energy loss to recoils per ion (eV)	Vacancy number per ion	Sensitivity ($Å^3$/ion)
			700 Å thick PMMA film				
He^+	43	9.6×10^{-21}	5592	72	188	3	5.6×10^5
Si^{++}	70	3.2×10^{-20}	11 810	5261	14 798	154	1.8×10^6
Ga^+	30	3.3×10^{-20}	2572	10 066	25 280	430	1.9×10^5
Au^{++}	70	8.6×10^{-20}	10 181	21 911	55 244	914	2.0×10^6
			2000 Å thick PMMA film				
He^+	43	9.6×10^{-21}	14 860	297	718	12	1.4×10^6
Si^{++}	70	3.2×10^{-20}	23 783	19 455	41 638	575	1.5×10^6
Ga^+	30	3.3×10^{-20}	2526	10 329	24 976	439	2.2×10^5
Au^{++}	70	8.6×10^{-20}	10 131	22 743	55 175	957	1.8×10^6

measurement and simulation. In general, the He^+ ion microscope has a higher spatial resolution, due to a smaller beam spot (3.5 Å in the instrument specifications) than that of Si^{++} ion microscope (80 Å in the instrument specifications). This is consistent with He^+ ions originating from a single atom of the trimer tip in the GFIS while Si^{++} ions from the Taylor cone in the LMIS. The helium ion microscope also has smaller lens aberrations, which enable a smaller beam spot. Furthermore, the trajectories of the He^+ ions and recoil atoms in the PMMA region are evidently more confined than those of the Si^{++} ions and recoil atoms in the simulation data. In spite of these inherent advantages of He^+ over Si^{++}, the developed lines for He^+ and Si^{++} are found to have similar widths. There exists therefore (ion, recoil atom, electron)-PMMA interaction that has a broader lateral range for He^+ than for Si^{++}. Our conclusion is that this could be due to He^+ ion-initiated electron cascade.

We have measured the dissolved area (in $Å^2$) in the cross-sectional image of the developed lines, and then divided it by the dose (in ions/Å) to obtain the PMMA sensitivity to the ion (in $Å^3$/ion), which corresponds to the soluble-in-developer volume caused by a single ion. We have also integrated the depth profiles for energy loss to electrons by ion (red), energy loss to electrons by recoils (blue) and vacancy number (magenta) in figure 2 (bottom panels) over the thickness of the PMMA film (up to 700 Å) to obtain the integrated energy losses to electrons by ion and by recoils, and the integrated vacancy numbers in the entire PMMA film, respectively. Similarly, we have calculated the integrated energy loss to recoil atoms by ion. These measured and calculated data for the He^+, Si^{++}, Ga^+ and Au^{++} ions are compared in table 1. Evidently, the energy loss to recoil atoms by ion, the energy loss to electrons by recoil atoms, and the vacancy number all increase with increasing mass of the ion. Not surprisingly, the lighter ions (He^+, Si^{++}) and ions with a higher energy (Si^{++}, Au^{++}) tend to lose more energy to the electrons. As for resist sensitivity, $Si^{++}$and Au^{++} ions provide the highest values (~2×10^6 $Å^3$/ion), which is nearly 3.5 times that of He^+, and ten times that of Ga^+. Between Si^{++} and Au^{++} ions, all the simulation data are found to be higher for Au^{++} than for Si^{++}, except for the energy loss to electrons by ion (of which Au^{++} is 15% lower than Si^{++}). In spite of this, Si^{++} ions have two advantages over Au^{++} ions in terms of resist sensitivity: the corresponding depth profile of the energy loss to electrons by ion (red curves in figure 2, bottom panels) has a much steeper slope for Au^{++} than for Si^{++}, indicating a faster drop in the energy imparting to electrons as the ion travels deeper into the PMMA film. The Si^{++} ion-initiated electron cascade therefore leads to more long-chain cleavage than the Au^{++} ion-initiated electron cascade in the PMMA film. Another advantage of the lighter ions over heavier ions is that the lighter ions could reach the Si substrate and further generate backscattered ions and electrons. A small extent of undercut observed in the He^+ and Si^{++} developed lines (figure 2, top panels) reveals this back scattering effect (often also known as the proximity effect). As the result of the favorable depth profile of the energy loss to electrons by ion and the backscattering effect for Si^{++}, the resist sensitivities for Au^{++} and Si^{++} ions are found to be similar, although the overall vacancy number generated by Au^{++} is six times of that by Si^{++}.

Since no backscattering (from the Si substrate) occurs for Ga^+ and Au^{++} ion exposures, we can compare their experimental and simulation results to deduce a semi-empirical relation that determines the resist sensitivity. The ratio of the resist sensitivity of Au^{++} to that of Ga^+ is 10.5 ($=2.0 \times 10^6/1.9 \times 10^5$). The closest value (8.4) in the simulation results can be obtained from the ratio of the product of energy loss to electrons by ion and the vacancy number [$(10\,181 \times 914)/(2572 \times 430)$]. This suggests that the resist sensitivity is proportionally dependent on the ion-initiated electron cascades (evaluated by energy loss to electrons by ion) and the number of ion- and recoil-induced vacancies. The value of the energy loss to electrons by recoils (that represents the recoil atom-initiated electron cascades) is not included in the product because the resulting ratio (18.3) would deviate too much from the experimental result (10.5). As the recoil atom-initiated electron cascade is considered a 'second-order' effect in terms of sequence and importance, it is not expected to play a major role in long-chain scissoring and is therefore not considered here. We also find good correlation between the resist sensitivity and the product of energy loss to electrons by

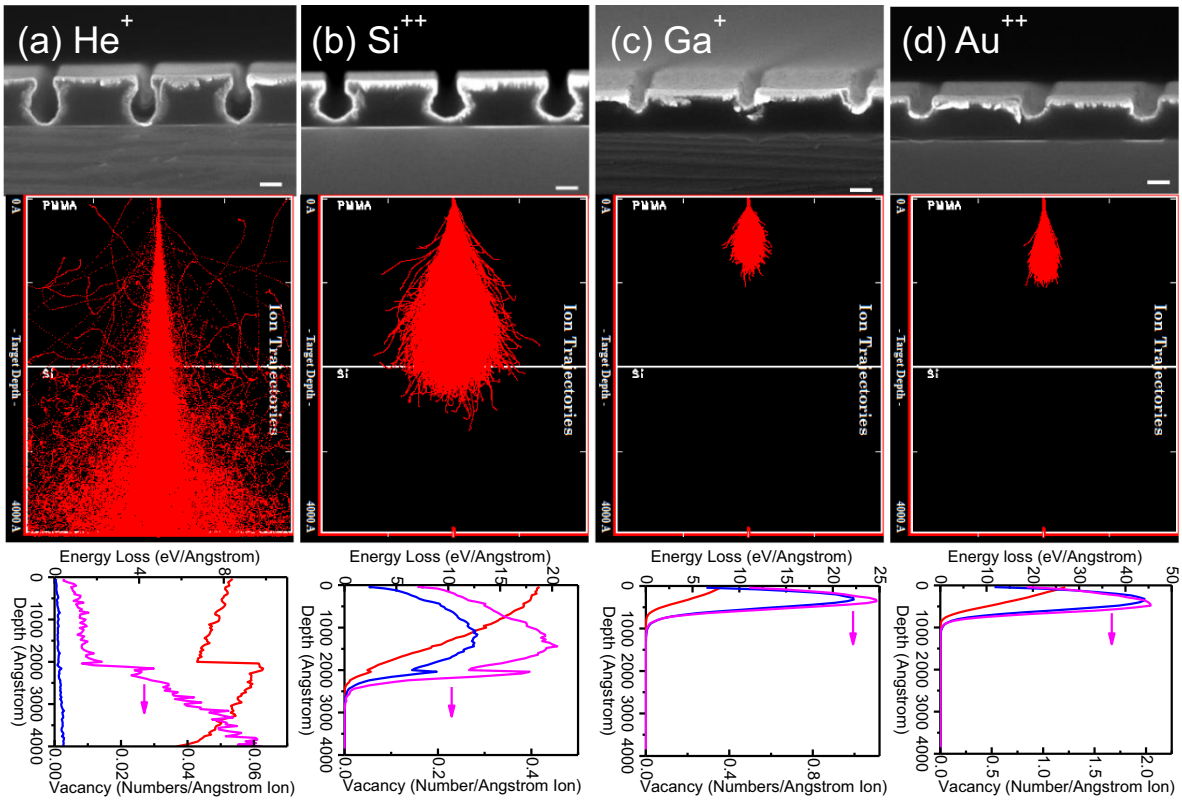

Figure 3. Top: SEM images of cross sections of developed lines on a 2000-Å thick PMMA film patterned by (a) He^{+} at 43 keV, dose: 1.8×10^{8} ions cm^{-1}; (b) Si^{++} at 70 keV, dose: 1.4×10^{8} ions cm^{-1}; (c) Ga^{+} at 30 keV, dose: 2.6×10^{8} ions cm^{-1}, and (d) Au^{++} at 70 keV, dose: 5.6×10^{7} ions cm^{-1}. The scale bar represents 100 nm. Middle: Simulated ion trajectories provided by TRIM. Bottom: Depth profiles of energy loss to electrons by ion (red), energy loss to electrons by recoil atoms (blue), and vacancy number (magenta).

ion and the vacancy number in the results for the 2000-Å thick PMMA film (table 1).

SEM images of the cross sections of the developed lines patterned on the 2000-Å thick PMMA film, together with the corresponding simulation results are shown in figure 3. The exposure doses are 1.8×10^{8}, 1.4×10^{8}, 2.6×10^{8}, and 5.6×10^{7} ions cm^{-1} for He^{+}, Si^{++}, Ga^{+} and Au^{++}, respectively. The ion trajectories of the four ion species are clearly dependent on their masses. For He^{+}, almost all the ions could penetrate the thicker film and are therefore able to expose the entire film. The He^{+} beam is also confined around the incident beam axis with the smallest lateral dispersion. For Si^{++}, only a small number of ions can reach the Si substrate, and the overall spatial extent of the ion trajectories forms a pear shape. For the heavier ions Ga^{+} and Au^{++}, their trajectories are nearly unchanged from those found in the 700-Å thick film, because their stopping ranges are less than 700 Å. Their lateral dispersions are small and even (except for the top 10%–20% depth). Since the ion-PMMA interaction depths in the 2000-Å thick film for He^{+} and Si^{++} are nearly three times of those in the 700-Å thick film, the extension and expansion of the interaction into the thicker film can be revealed.

In contrast to the similar trench shape in the 700-Å thick film found for all the ion species, the cross-sectional shapes of the lines are quite different in the 2000-Å thick film: pear shape for He^{+}, Florence flask shape for Si^{++}, and trench shape for Ga^{+} and Au^{++}. These differences in the cross-sectional shapes are the result of different ion-PMMA interaction processes and volumes, which can be analysed with the aid of the TRIM simulation. The calculated data from the simulation are compared in table 1. As we have demonstrated above, the ion-initiated electron cascades and the ion- and recoil-induced vacancies are mainly responsible for the long-chain scissoring. The ion-initiated electron cascade is expected to have a similar shape as the primary electron-initiated (secondary) electron cascade in matter. It is known that the scattering of primary electrons in matter displays pear shape. Indeed, we observe similar pear-shaped cross sections after the same lines are exposed using a 10 keV electron beam on the 2000-Å thick PMMA film (see supporting information (avaliable online at stacks.iop.org/Nano/31/325301/mmedia) on SEM cross-sectional imaging of the developed lines, and the Monte Carlo simulation result of the electron beam in PMMA film). The depth profile of the vacancy number (magenta curve) can be obtained from TRIM simulation. In figure 3, we also observe the pear-shaped cross sections of the He^{+} exposed lines. Together with the negligible vacancy number caused by a He^{+} ion (12, table 1), these results indicate that long-chain scissoring is accomplished predominantly by the ion-initiated electron cascade. For a He^{+} ion, its overall energy loss to electrons by ion is the second largest (only smaller than that for Si^{++}). For Si^{++}, the cross-sectional shape, with the round bottom being much wider, is more akin to that of a Florence flask rather than a pear. As the pear shape mainly results from the

ion-initiated electron cascade, the widening in the thicker film near 1400 Å is related to the large vacancy number induced by the recoil atom cascade. Indeed, the depth profile of the vacancy number (magenta curve) exhibits a peak at 1440 Å. Meanwhile, the peaks in the depth profiles of the vacancy numbers for Ga^{+} and Au^{++} are found to be located at considerably smaller depths (360 and 500 Å, respectively), but their corresponding cross-sectional shapes are trench-like with relatively straight side walls and no apparent widening at the corresponding depth (figure 3, top panels). This is likely due to the small depth of the developed lines, in which the overlap of the expansion ranges of the scattered electrons, ions and atom recoils are relatively even around the incident beam axis. Straight vertical edges are also observed on the top parts of the developed lines in the thicker films for He^{+} and Si^{++}.

The resist sensitivity is mainly related to the ion-initiated electron cascade, ion- and recoil-induced vacancies, and also to the backscattering effect for light ions (He^{+}). The resist sensitivities to the heavier ions (Si^{++}, Ga^{+} and Au^{++}) in the 2000-Å thick film are generally similar to those in the 700-Å thick film. For He^{+}, however, its resist sensitivity for the thicker film is 2.5 times that for the thinner film (table 1). We attribute this increase in resist sensitivity to the larger range of the ion-initiated electron cascade and the higher number of vacancies as a result of the longer travelling distance of a He^{+} ion available in the thicker film. This allows the lighter ion to cause long-chain scissoring over the available greater depth in the thicker film before leaving the resist and entering the substrate. For the 2000-Å thick film, the ratio of resist sensitivity for Au^{++} to Ga^{+} (8.2) is found to be in good accord with the ratio of the products of their respective energy losses to electrons by ion and vacancy numbers (8.7). This semi-empirical relation is therefore applicable to both the thicker film and the 700-Å thick film (observed previously). This confirms that the long-chain scissoring capability is proportional to the ion-initiated electron cascade and the ion- and recoil-induced vacancies for Ga^{+} and Au^{++}. However, the ratio of resist sensitivity to Au^{++} to that to He^{+} (1.3) is significantly smaller than the ratio of the products of their respective energy losses to electrons by ion and vacancy numbers (54). This could be due to underestimate of the long-chain scissoring capability of the He^{+} ion-initiated electron cascade. The energy loss to electrons by ion decreases with increasing depth at a much faster rate for Au^{++} than for He^{+}, as shown in their respective depth profiles (red curves in figure 3, bottom panels). On the other hand, the ratio of resist sensitivity for Au^{++} to Si^{++} (1.2) is larger than the ratio of the products of their respective energy losses to electrons by ion and vacancy numbers (0.7), which suggests overestimate of the long-chain scissoring capability of the Si^{++} ion-initiated electron cascade. Apparently, the Si^{++} ion-initiated electron cascade deeper in the film causes less long-chain cleavage than those generated close to the film surface.

4. Concluding remarks

We have studied simple line patterns generated by ion beam lithography by exposure of several commonly accessible ions (He^{+}, Si^{++}, Ga^{+} and Au^{++}) on a 700-Å thick and a 2000-Å thick PMMA resist films supported on Si substrates, and compared the experimental results with the TRIM simulation. From the resist sensitivity and the cross-sectional shape of the developed lines, we conclude that in the ion-PMMA interaction process, long-chain scissoring is mainly accomplished by ion-initiated electron cascades and ion-induced recoil atom cascades, which can be evaluated respectively by energy loss to electrons by ion and vacancy distribution in the TRIM simulation. For heavy ions, we obtain a semi-empirical relation between the resist sensitivity and the product of the energy loss to electrons by ion and the vacancy number. The ion-initiated electron cascade occurs over the entire depth for He^{+} and contributes more to long-chain scissoring than those for the heavier ions. The lightest ion species, He^{+}, therefore offers the best ion source for ion beam lithography for the thicker (2000-Å) PMMA resist film, which could become important for patterns that require a thick metallization layer. On the other hand, Au^{++} provides the highest resist sensitivity because of the largest vacancy number generated in the recoil atom cascade. Of the four ions considered here, Au^{++} therefore provides the most efficient source for exposing large-area patterns on a thinner PMMA resist. Since high energy ion-matter interaction induces recoil atom cascades and generates vacancies, which does not occur in electron- or photon-matter interaction, new types of resist materials could potentially be developed specifically for ion beam lithography.

Acknowledgments

This work was supported by the Natural Sciences and Engineering Research Council of Canada.

ORCID iD

Kam Tong Leung https://orcid.org/0000-0002-1879-2806

References

[1] Bruchhaus L, Mazarov P, Bischoff L, Gierak J, Wieck A and Hövel H 2017 Comparison of technologies for nano device prototyping with a special focus on ion beams: a review *Appl. Phys. Rev.* **4** 011302
[2] Gierak J 2009 Focused ion beam technology and ultimate applications *Semicond. Sci. Technol.* **24** 043001
[3] Ocola L, Rue C and Maas D 2014 High-resolution direct-write patterning using focused ion beams *MRS Bull.* **39** 336–41
[4] Volkert C and Minor A 2007 Focused ion beam microscopy and micromachining *MRS Bull.* **32** 389–95
[5] Bassim N, Scott K and Giannuzzi L 2014 Recent advances in focused ion beam technology and applications *MRS Bull.* **39** 317–25
[6] Tseng A 2004 Recent developments in micromilling using focused ion beam technology *J. Micromech. Microeng.* **14** R15–R34
[7] Livengood R, Winer P and Rao V 1999 Application of advanced micromachining techniques for the characterization and debug of high performance microprocessors *J. Vac. Sci. Technol.* B **17** 40–43

[8] Ward B, Notte J and Economou N 2006 Helium ion microscope: a new tool for nanoscale microscopy and metrology *J. Vac. Sci. Technol.* B **24** 2871–4
[9] Economou N, Notte J and Thompson W 2012 The history and development of the helium ion microscope *Scanning* **34** 83–89
[10] Swanson L 1983 Liquid metal ion sources: mechanism and applications *Nucl. Instr. Meth.* **218** 347–53
[11] Orloff J 1987 Comparison of optical design approaches for use with liquid metal ion sources *J. Vac. Sci. Technol.* B **5** 175–7
[12] Van Es J, Gierak J, Forbes R, Suvorov V, Van den Berghe T, Dubuisson P, Monnet I and Septier A 2004 An improved gallium liquid metal ion source geometry for nanotechnology *Microelectron. Eng.* **73–4** 132–8
[13] Bischoff L, Mazarov P, Bruchhaus L and Gierak J 2016 Liquid metal alloy ion sources-an alternative for focused ion beam technology *Appl. Phys. Rev.* **3** 021101
[14] Beale M, Broughton C and Deshmukh V 1986 Focused ion beams for lithography and direct doping in VLSI device fabrication *Microelecctron. Eng.* **4** 233–49
[15] Kubena R, Ward J, Stratton F, Joyce R and Atkinson G 1991 A low magnification focused ion beam system with 8 nm spot size *J. Vac. Sci. Technol.* B **9** 3079–83
[16] Bruchhaus L, Bauerdick S, Peto L, Barth U, Rudzinski A, Mussmann J, Klingfus J, Gierak J and Hövel H 2012 High resolution and high density ion beam lithography employing HSQ resist *Microelectron. Eng.* **97** 48–50
[17] Li W, Wu W and Williams R 2012 Combined helium ion beam and nanoimprint lithography attains 4 nm half-pitch dense patterns *J. Vac. Sci. Technol.* B **30** 06F304
[18] Mohammad M, Muhammad M, Dew S and Stepanova M 2012 Fundamentals of electron beam exposure and development *Nanofabrication*, ed M Stepanova and S Dew (Berlin: Springer) pp 11–41
[19] Ziegler J 2015 SRIM (avaliable at:www.srim.org)
[20] Zhang L, Heinig N, Bazargan S, Abd-Ellah M, Moghimi N and Leung K T 2015 Direct-write three-dimensional nanofabrication of nanopyramids and nanocones on Si by nanotumefaction using a helium ion microscope *Nanotechnology* **26** 255303
[21] Bauerdick S, Bruchhaus L, Mazarov P, Nadzeyka A, Jede R, Fridmann J, Sanabia J, Gila B and Appleton B 2013 Multispecies focused ion beam lithography system and its applications *J. Vac. Sci. Technol.* B **31** 06F404